

Catalysis under shell: Improved CO oxidation reaction confined in Pt@h-BN core-shell nanoreactors

Mengmeng Sun¹, Qiang Fu¹ (✉), Lijun Gao^{1,2}, Yanping Zheng³, Yangyang Li³, Mingshu Chen³, and Xinhe Bao¹

¹State Key Laboratory of Catalysis, iChEM, Dalian Institute of Chemical Physics, Chinese Academy of Sciences, Dalian 116023, China

²Department of Chemical Physics, University of Science and Technology of China, Hefei 230026, China

³State Key Laboratory of Physical Chemistry of Solid Surfaces, Department of Chemistry, Xiamen University, Xiamen 361005, China

Received: 7 January 2017

Revised: 25 January 2017

Accepted: 3 February 2017

© Tsinghua University Press
and Springer-Verlag Berlin
Heidelberg 2017

KEYWORDS

core-shell,
CO oxidation,
Pt,
hexagonal boron nitride,
nanoreactor

ABSTRACT

Core-shell nanostructures consisting of active metal cores and protective shells often exhibit enhanced catalytic performance, in which reactants can access a small part of the core surfaces through the pores in the shells. In this study, we show that Pt nanoparticles (NPs) can be embedded into few-layer hexagonal boron nitride (h-BN) overlayers, forming Pt@h-BN core-shell nanocatalysts. The h-BN shells not only protect the Pt NPs under harsh conditions but also allow gaseous molecules such as CO and O₂ to access a large part of the Pt surfaces through a facile intercalation process. As a result, the Pt@h-BN nanostructures act as nanoreactors, and CO oxidation reactions with improved activity, selectivity, and stability occur at the core-shell interfaces. The confinement effect exerted by the h-BN shells promotes the Pt-catalyzed reactions. Our work suggests that two-dimensional shells can function as robust but flexible covers on nanocatalyst surfaces and tune the surface reactivity.

1 Introduction

Pt-based nanostructures are widely used in many important catalytic processes, such as fuel cells, hydrogenation/dehydrogenation reactions, and CO oxidation reactions [1–3]. Although these nanocatalysts often show extraordinary activity, they present challenges. First, Pt-based nanoparticles (NPs) are susceptible to high-temperature sintering in gas phase reactions and electrochemical leaching in electrocatalytic reactions, which reduce the density of the active sites [4–6]. Second, CO, sulfur-containing molecules, and

other impurities introduced in reactions contaminate the catalysts owing to the strong adsorption of these molecules on the surfaces [7–9]. Third, a relatively low selectivity is exhibited by this group of catalysts because they exhibit equally high activity for many reactions [10–12]. These limitations of the catalysts, as well as their high cost, have spurred considerable interest in designing Pt-based nanocatalysts with new structural configurations.

In the past decades, considerable progress has been made to solve these critical issues. For example, 3d transition metals have been alloyed with Pt to form

Address correspondence to qfu@dicp.ac.cn

Pt-based bi- and tri-metallic catalysts, which exhibit higher activity and stability in electrocatalytic reactions [2, 13–16]. Pt nanocatalysts can be combined with nanosize oxides, nitrides, and carbides, yielding Pt-based nanocomposites with enhanced catalytic performance [3, 17–20], in which the strong metal–support interaction effect plays an important role [21, 22]. The catalytic properties of Pt-group NPs have been improved by encapsulation within inorganic shells; here, porous shells are needed to allow access to a small part of the active surfaces [4, 16, 23–26]. All of these routes can solve one or at most two of the three critical issues for heterogeneous catalysis (activity, selectivity, and stability).

Recently, we demonstrated that the space between the two-dimensional (2D) overlayer and the metal surface can act as a 2D nanoreactor. Small molecules such as CO, O₂, NH₃, and H₂ intercalate the 2D overlayers and react with each other on the underlying metal surfaces [27–35]. Surface science studies confirm that metal-catalyzed reactions can be significantly enhanced by the confinement effect of the 2D covers, and the concept of “catalysis under 2D cover” is well-established [33, 36–39]. We suggest that this concept can be applied to supported nanocatalysts via the construction of metal nanocatalysts encapsulated with 2D shells, in which nanoreactors form between the 2D shells and the metal cores. Both the activity and selectivity of the reactions occurring inside the core–shell nanoreactors can be improved by the confinement effect of the shell covers. Moreover, the protective shells prevent the metal NPs from sintering, enhancing their stability.

In this study, we employed a facile strategy to embed Pt NPs into hexagonal boron nitride (h-BN) layers. The Pt@h-BN core–shell structures were confirmed by high-sensitivity low-energy ion scattering spectroscopy (HS-LEIS), high-resolution transmission electron microscopy (HRTEM), and X-ray photoelectron spectroscopy (XPS). C-supported Pt@h-BN catalysts (Pt@h-BN/C) were used for CO oxidation, and higher oxidation activity was observed compared with the Pt/C catalyst. Because of the geometric constraints of the core–shell nanoreactors, only CO oxidation occurred—not propene oxidation—and the core–shell catalysts exhibited high selectivity. The Pt NPs were

protected by the robust h-BN shells, which had high stability. The encapsulation of metal NPs by 2D materials was demonstrated as an effective strategy for improving the catalytic performance of Pt-based catalysts.

2 Results and discussion

Pt@h-BN/C catalysts were synthesized through a well-established process, as illustrated in Fig. 1(a). In the first step, ammonia borane (AB, NH₃BH₃) dehydrogenation occurred preferentially on the Pt surfaces owing to their catalytic effect, and the formed insoluble polymerization products (p-AB, [BH_xNH_y]_n) encapsulated the Pt NPs (Pt@p-AB/C) [40, 41]. The polymer coatings were subjected to further dehydrogenation via heating at 500 or 700 °C in a NH₃ atmosphere and formed h-BN shell layers on top of the Pt NPs (Pt@h-BN/C).

XPS was performed to examine the surface composition during the preparation process. The B 1s and N 1s spectra of the samples before and after the pyrolysis in NH₃ are shown in Figs. 1(b) and 1(c). All the B 1s spectra can be fitted using two components, which correspond to h-BN at 190.8 eV [42, 43] and sub-stoichiometric boron oxide (BO_x) species around 192.4 eV [44, 45]. For the Pt@p-AB/C sample, the B 1s spectrum is dominated by the 192.4 eV component because the p-AB coatings were susceptible to hydrolysis in air and most of the B atoms were bonded with O [46]. The B 1s spectrum of the Pt@h-BN/C-700 sample mainly consists of the B–N component, indicating that the pyrolysis in NH₃ at elevated temperatures transformed the B–O bonds into B–N bonds. A similar trend is observed in the N 1s spectra. The N 1s spectrum for the Pt@p-AB/C sample contains three components, at 398.3 eV (assigned to N–B bonding), 400.2 eV (assigned to N–H bonding), and 402.1 eV (assigned to N–O bonding) [42, 43, 47, 48]. Upon high-temperature treatments in NH₃, the N–H signals were strongly attenuated, and only the N–B signal was observed for the Pt@h-BN/C-700 sample. XPS revealed the transformation from p-AB to h-BN on the Pt surfaces when the samples were heated in a NH₃ atmosphere.

HS-LEIS reveals the atomic composition of the

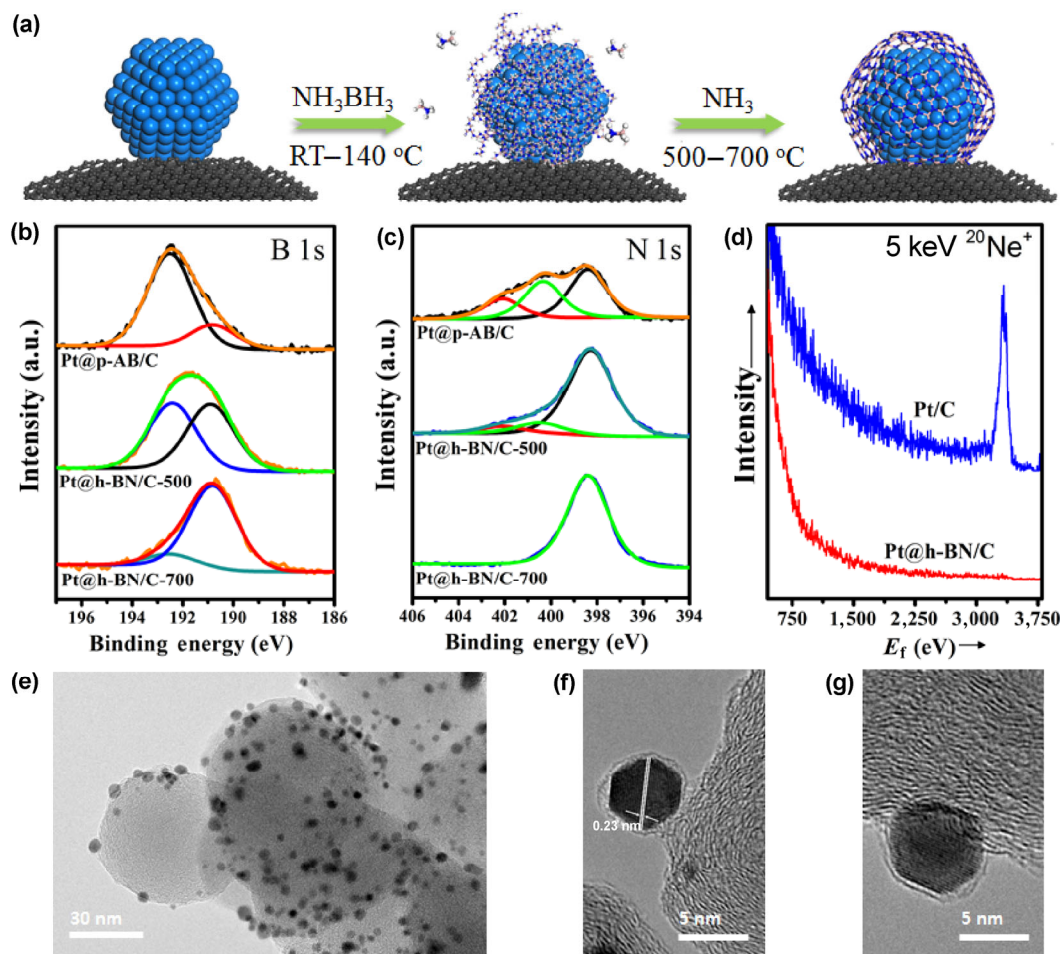


Figure 1 Preparation and characterization of the Pt@h-BN nanocatalysts. (a) Schematic of the preparation process; (b) and (c) XPS B 1s and N 1s spectra of the Pt@p-AB/C, Pt@h-BN/C-500, and Pt@h-BN/C-700 catalysts; (d) HS-LEIS spectra of the Pt/C and Pt@h-BN/C-500 catalysts; TEM and HRTEM images of the Pt@h-BN/C-500 catalyst (e) and (f) and Pt@h-BN/C-700 catalyst (g).

outermost surface layers of solids [49]. The HS-LEIS spectra for the Pt/C and Pt@h-BN/C samples are shown in Figs. 1(d) and Fig. S1 in the Electronic Supplementary Material (ESM). For the Pt/C sample, a strong Pt signal is observed in the spectrum, as all the Pt NPs were bared. In contrast, for the Pt@h-BN/C sample, almost no Pt signal was detected, but B and N peaks appeared. We conclude that most of Pt NPs were fully coated by h-BN overlayers, forming Pt@h-BN core-shell nanostructures.

Although the Pt@h-BN/C samples were subjected to high-temperature treatment, their particle-size distribution was similar to that of the Pt/C catalyst. TEM images of the Pt@h-BN/C and Pt/C samples are shown in Fig. 1(e) and Fig. S2(a) in the ESM, respectively, and their average particle sizes were

measured to be ~2.5 nm. Both the p-AB coating layers and the h-BN shells formed on the Pt NPs effectively prevented particle growth during the pyrolysis. Energy-dispersive X-ray spectroscopy element-mapping images show that B and N had the same spatial distribution in the sample (Fig. S3(a) in the ESM). HRTEM images of the Pt@h-BN/C samples (Figs. 1(f) and 1(g)) show clear lattice fringes in the particles with a distance of 0.23 nm, which is consistent with the *d*-spacing of the (111) planes of face-centered cubic Pt. Moreover, the large quantity of NPs on the C support indicates that most of the Pt NPs were coated with ultrathin graphitic h-BN layers. The graphitization degree of the h-BN shells increased with the ammonolysis temperature (Figs. 1(f) and 1(g), and Figs. S2(d)–S2(i) in the ESM). TEM provided

further evidence of the formation of the Pt@h-BN core-shell nanostructures. The coverage of the h-BN shells was controlled according to the AB/Pt ratio. The Pt and B contents in the Pt@h-BN/C catalysts were measured via microwave digestion and inductively coupled plasma optical emission spectroscopy. The B content increased with the AB/Pt ratio (Fig. S3(b) in the ESM). Unless otherwise specified, the Pt@h-BN/C samples discussed below were prepared at an ammonolysis temperature of 500 °C and an AB/Pt ratio of 20.

Pt/C and Pt@h-BN/C samples were subjected to annealing at 850 °C in N₂ for 1 h, and the Pt particle size and morphology were investigated using X-ray diffraction (XRD) and TEM. As shown in Fig. 2(a), the particle size of the Pt/C sample, which was calculated according to the main diffraction peak, increased from 2.3 to 5.2 nm after the sintering. In contrast, the Pt@h-BN/C sample retained its small particle size (3.5 nm). TEM images of the treated Pt/C and Pt@h-BN/C samples show the difference in the particle size more clearly (Figs. 2(b) and 2(c), and Fig. S4 in the ESM). Figure 2(b) shows that the Pt NPs in the treated Pt/C sample were well-dispersed on the C support, but many large NPs close to 10 nm in size were observed. The morphology of the Pt particles in the treated Pt@h-BN/C sample did not change significantly (Fig. 2(c)). Both XRD and TEM revealed

no strong particle growth in the Pt@h-BN/C sample during the high-temperature sintering process, which suggests that the h-BN shells effectively protected the Pt cores from thermal aggregation.

In addition to the thermal stability of Pt catalysts, the chemical stability of the C support in Pt/C catalysts is a critical issue for the catalytic performance [50, 51]. To address this, temperature-programmed oxidation (TPO) experiments were performed on the Pt/C and Pt@h-BN/C samples. As shown in Fig. 2(d), there was only one sharp peak—centered at 400 °C—for the Pt/C sample, which was due to oxidation of the C support with the aid of the catalysis of the Pt NPs. This oxidation peak shifted to 428 °C for the Pt@h-BN/C sample and 512 °C for the Pt@h-BN₁₀/C sample. For the Pt@h-BN₂₀/C sample, there was a wide TPO peak similar in shape to the TPO signal from the pure XC-72 C support [52]. Apparently, the h-BN shells separated the Pt NPs from the C support, suppressing the activation of O₂ and blocking the O₂ spillover from the Pt to the support surfaces. The oxidation of the C supports in the Pt/C and Pt@h-BN/C samples in air were examined *in situ* using Raman spectroscopy (Fig. S5 in the ESM). Upon heating to 498 °C, both the D and G bands at 1,350 and 1,590 cm⁻¹—which are characteristic of the C support in the Pt/C sample—completely disappeared. These two bands remained when the Pt@h-BN/C sample was heated above 572 °C.

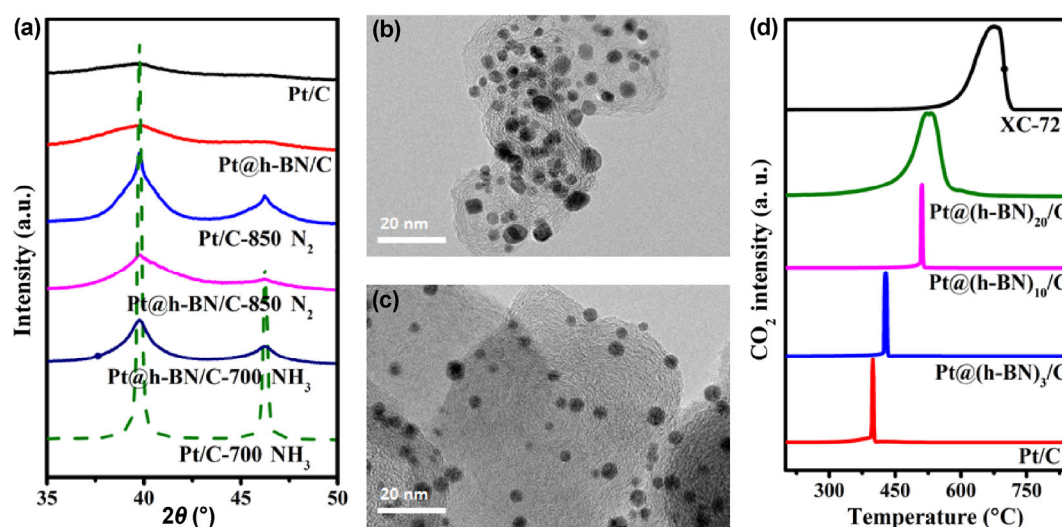


Figure 2 Stability of the Pt@h-BN/C catalysts. (a) XRD patterns of the Pt/C and Pt@h-BN/C samples subjected to different heating treatments; TEM images of Pt/C (b) and Pt@h-BN/C (c) samples treated in N₂ at 850 °C; (d) TPO profiles of the XC-72, Pt/C, and Pt@h-BN/C samples.



In situ Raman investigations confirmed the results of the TPO experiments.

When the catalysts were treated in NH_3 at high temperatures, the C support was etched by dissociated H species, resulting in Pt particle aggregation. For the Pt/C sample treated in NH_3 at 700 °C, the Pt particle size increased to 34.3 nm. The Pt@h-BN/C sample was treated under the same conditions, and its NPs retained their size of ~4.7 nm (Fig. 2(a)). Again, the h-BN shells suppressed H_2 spillover from the Pt to the C support, contributing to the significant improvement in the thermal stability of the C support in NH_3 and H_2 .

Comparative CO chemisorption analyses on the Pt/C and Pt@h-BN/C samples were conducted using CO pulse chemisorption. The measured chemisorption uptakes are shown in Fig. 3(a). All the Pt@h-BN/C catalysts exhibited considerable CO chemisorption, although most of the Pt NPs in the Pt@h-BN/C samples were embedded by h-BN overlayers. The CO adsorption on the Pt/C and Pt@h-BN/C catalysts was further investigated by *in situ* infrared (IR) spectroscopy (Fig. 3(b)). When exposed to CO at room temperature, the two catalysts exhibited strong peaks at 2,091 and 2,082 cm^{-1} due to the CO adsorbed on the Pt [28, 53]. The significant CO adsorption for these catalysts confirms that the CO molecules were intercalated

in the ultrathin h-BN shells and adsorbed on the Pt surfaces underneath, which is similar to results for the intercalation of CO in graphene and h-BN overlayers supported on planar metal surfaces [27, 28, 54–58]. The penetration of CO molecules through the h-BN shells has to make use of the defect sites in the h-BN overlayers, including domain boundaries, vacancies, and edges, which function as diffusion channels for the intercalation of molecules in the graphitic overlayers [31, 59–62].

CO temperature-programmed desorption (TPD) experiments were performed for the CO-saturated Pt/C and Pt@h-BN/C catalysts (Fig. 3(c)). The Pt/C sample exhibited a wide desorption peak centered around 254 °C, which is typical for pure Pt nanocatalysts [63]. With a small amount of h-BN layers coated on the Pt NPs, i.e., in the case of the Pt@(h-BN)₃/C sample, little difference was observed in the TPD spectra. However, the TPD signal acquired from the Pt@(h-BN)₁₀/C sample exhibited two peaks: a low-temperature peak at 95 °C and a high temperature peak at 290 °C. For the Pt@(h-BN)₂₀/C sample, only the low-temperature peak was present. The CO chemisorption and *in situ* IR data confirm that the CO was intercalated in the h-BN shells. Therefore, the CO molecules adsorbed on the Pt@h-BN/C surface consisted of the CO molecules on the bared Pt surfaces

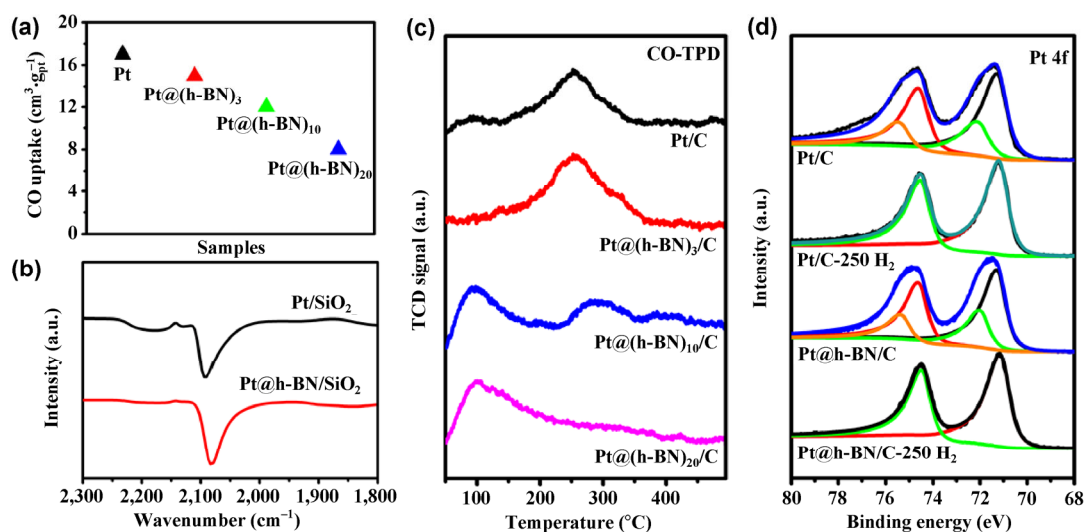


Figure 3 Chemisorption of CO and O_2 for the Pt@h-BN/C catalysts. (a) CO uptake for the Pt/C and Pt@h-BN/C catalysts from CO pulse chemisorption around 50 °C. (b) *In situ* IR spectra of CO adsorbed on the Pt and Pt@h-BN catalysts. For the IR measurements, both catalysts were supported on SiO_2 . (c) CO TPD spectra of the Pt/C and Pt@h-BN/C catalysts; (d) XPS Pt 4f spectra of the Pt/C and Pt@h-BN/C catalysts under various treatment conditions.

and those sitting between the h-BN shells and the Pt surfaces. As previously discussed, the high-temperature desorption peak originated from the CO on the bared Pt surfaces, and the low-temperature TPD peak originated from the CO at the core-shell interfaces. As the h-BN coverage increased, the low-temperature peak became more dominant, which confirms this assertion. The fact that the CO desorption from the h-BN/Pt interface occurred at the lower temperature reveals the confinement effect of the 2D cover, which weakened the CO adsorption on the Pt surface [27, 28].

The XPS Pt 4f spectra were recorded for the Pt/C and Pt@h-BN/C samples, which were exposed to air after the reduction treatment and then transferred to the XPS chamber (Fig. 3(d)). The deconvoluted spectra indicate the presence of Pt–O signals on the as-loaded samples. *In situ* reduction of the samples in H_2 at 250 °C completely removed the Pt–O component, and only the Pt–Pt component remained in the spectra. XPS results suggest that the O atoms were adsorbed on the Pt surfaces coated by the h-BN shells under ambient conditions, which should occur through the intercalation process as well.

Both the structural characterization and surface-adsorption data indicate that the formed Pt@h-BN core-shell structures functioned as nanoreactors; i.e., reactant molecules easily diffused into the core-shell interfaces and reacted with each other therein. The catalytic activity of the Pt/C and Pt@h-BN/C catalysts was evaluated using CO oxidation under the same conditions. Figure 4(a) shows the CO conversion for these catalysts. Interestingly, the Pt@h-BN/C catalysts exhibited better activity than the Pt/C catalyst at a low temperature. The Pt@(h-BN)₂₀/C catalyst exhibited 100% CO conversion at 94 °C, which is substantially lower than the corresponding temperature for the Pt/C catalyst. The Pt@p-AB/C sample exhibited complete CO conversion at 140 °C. Its low CO-oxidation activity is attributed to the blockage of the surface Pt sites with the coated polymer layers. To investigate the intrinsic activities of the Pt/C and Pt@h-BN/C catalysts, a CO oxidation reaction was conducted at a specific gas hourly space velocity (GHSV) with the CO conversion below 15%. Figure 4(b) shows Arrhenius plots of the CO conversion rate with respect to the inverse reaction temperature. The apparent reaction barriers

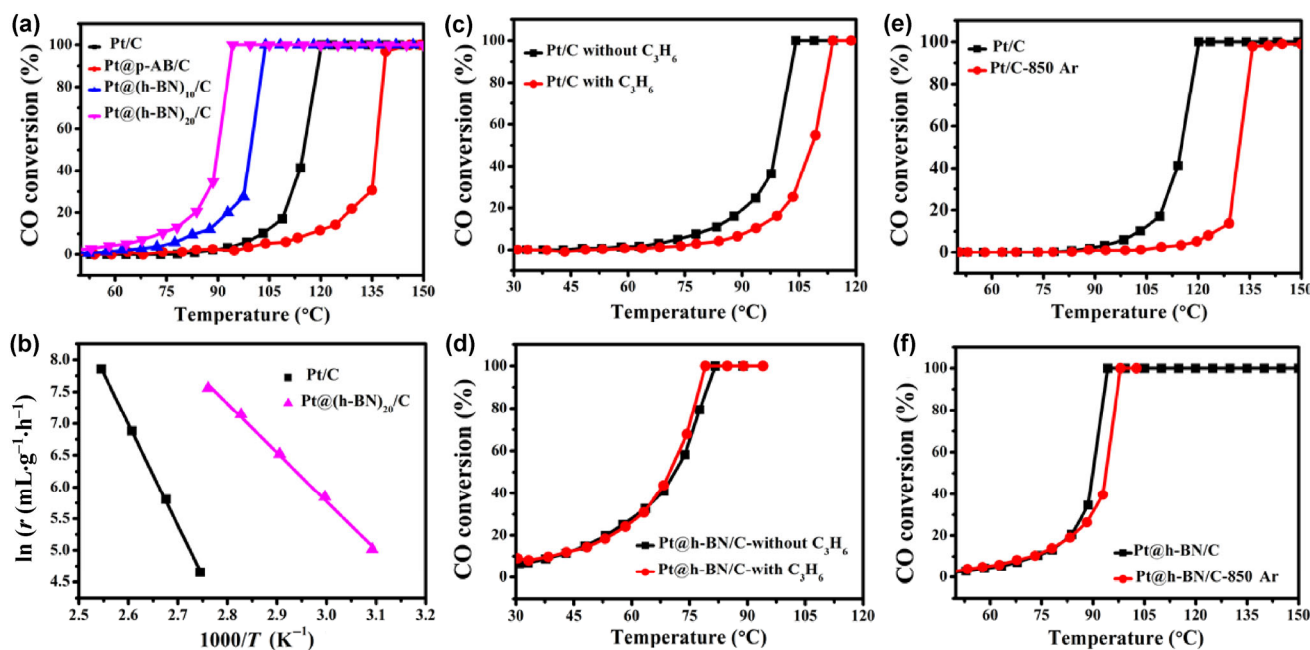


Figure 4 CO oxidation for the Pt/C and Pt@h-BN/C catalysts. (a) CO conversions for the CO oxidation on the Pt/C, Pt@p-AB/C, and Pt@h-BN/C catalysts (1% CO, 20% O₂, and He balance; GHSV = 552,000 mL·g_{Pt}^{−1}·h^{−1}); (b) Arrhenius plots of the CO oxidation rate for the Pt/C and Pt@h-BN/C catalysts; (c) and (d) CO oxidation with and without 0.2% C₃H₆ (red and black, respectively) for pure Pt/C and Pt@h-BN/C (GHSV = 154,000 mL·g_{Pt}^{−1}·h^{−1}); (e) and (f) CO oxidation before and after the high-temperature treatment of the Pt/C and Pt@h-BN/C catalysts in Ar for 1 h (GHSV = 552,000 mL·g_{Pt}^{−1}·h^{−1}).

were derived as 128 and 64 kJ·mol⁻¹ for the Pt/C and Pt@(h-BN)₂₀/C catalysts, respectively. The improved activity of the Pt@h-BN/C catalysts for the preferential oxidation of CO in the presence of H₂ (PROX) was observed (Fig. S6 in the ESM). All the reaction results indicate that the Pt NPs covered with h-BN shells exhibited higher CO-oxidation activity than the pure Pt catalyst, which accords with results for h-BN/Pt(111) model catalysts [28].

It is expected that the intercalation process is facile for small molecules such as CO, H₂, O₂, and H₂O but difficult for large molecules [31]. The intercalation channels may be limited for large molecules such as propene (C₃H₆), inhibiting reactions involving these big molecules. To confirm this, a control experiment involving selective CO oxidation in the presence of alkenes, which is a scientific and technical challenge, was performed [64, 65]. We included 0.2% C₃H₆ in the reaction gas, and the same CO oxidation reaction was conducted (Figs. 4(c) and 4(d)). The Pt/C catalyst exhibited a significant loss in activity with C₃H₆, whereas the reaction was almost unaffected by introducing C₃H₆ using the Pt@h-BN/C catalyst. The inhibitory effect of the hydrocarbons on the CO oxidation for the Pt-based catalysts is attributed to the competitive adsorption of the reactants on the surface active sites. The C₃H₆ molecules were difficult to intercalate in the h-BN shells; thus, the active Pt sites were free from C₃H₆ contamination.

We also investigated the effect of the thermal stability of both the catalysts on the CO oxidation. The catalysts were treated in flowing Ar at 850 °C for 1 h, and then CO oxidation reactions were conducted for the treated catalysts between room temperature and 150 °C (Figs. 4(e) and 4(f)). The Pt/C catalyst exhibited a significant loss in activity after the high-temperature treatment. In contrast, the CO-oxidation activity of the Pt@h-BN/C catalyst decreased very slightly after the same treatment. In combination with the stability experiment shown in Figs. 2(a)–2(c), the results confirm that the h-BN shells prevented the metal NPs from sintering and improved the reaction stability.

The aforementioned results indicate that the Pt NPs were effectively encapsulated by the few-layer h-BN shells through the simple preparation procedure.

Molecules such as CO and O₂ were intercalated in the BN overlayers and adsorbed on the metal surfaces underneath. The core–shell interfaces in the Pt@h-BN catalysts functioned as nanoreactors, in which the metal catalyzed the reactions occurring under the shells (Fig. 5(a)). In conventional core–shell nanocatalysts consisting of metal cores and porous oxide shells, the buried core–shell interfaces are inaccessible to reactants, and reactions occur on a small part of the metal surfaces, which are exposed to the pores in the shell (Fig. 5(b)). The difference between the two core–shell nanocatalysts was due to the fact that 2D shells such as h-BN and graphene interact weakly with metal surfaces, allowing molecules to intercalate into the core–shell interfaces and react under the shells.

In the Pt@h-BN core–shell nanoreactors, the shells exhibited a strong confinement effect on the surface chemistry and catalysis of the metal cores. First, the molecular adsorption on the Pt surface was weakened by the h-BN shell, as indicated by the lower CO desorption temperature in the TPD data. The weakened CO adsorption on the Pt alleviated the CO contamination and promoted the Pt-catalyzed CO oxidation, as demonstrated by our reaction data. Second, the molecular diffusion into and out of the nanoreactors exploited the defect sites of the h-BN shells, e.g., the domain boundaries and vacancies, which allowed the Pt@h-BN/C catalysts to perform reactions with high selectivity. Third, the Pt NPs were well-protected by the robust 2D shells, which were free from sintering at high temperatures. Overall, the encapsulation of

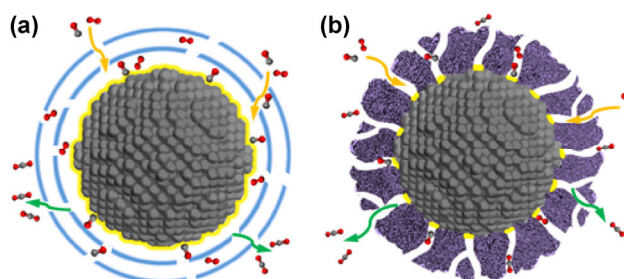


Figure 5 Reactions for the core–shell nanocatalysts. (a) Nanoreactor between the 2D shell and the metal core, in which most of the metal-core surface is accessible to the reactants; (b) reactions for the conventional core–shell nanocatalysts, in which only a small part of the metal surface exposed to the pores in the shell is active. The yellow lines on the core surfaces indicate the active surface regions. CO oxidation is used as the model reaction.

metal NPs with 2D shells can be regarded as an effective method for improving the catalytic performance.

3 Conclusions

Pt@h-BN core-shell nanostructures comprising Pt NPs covered by few-layer h-BN overlayers were synthesized via the catalytic dehydrogenation of NH_3BH_3 on Pt and subsequent ammonolysis. Surface-chemistry characterization confirmed that the CO and O_2 molecules were adsorbed on the Pt surfaces underneath the h-BN shells, which was facilitated by molecular intercalation in the h-BN overlayers. The Pt@h-BN core-shell nanostructures functioned as nanoreactors, in which CO oxidation occurred at the interfaces between the h-BN shells and the Pt cores with a lower apparent activation barrier than that of bare Pt catalysts. The confinement effect of h-BN shells endowed the Pt@h-BN catalysts with high selectivity in CO oxidation with the presence of hydrocarbons, as well as high stability at high temperatures.

Acknowledgements

This work was financially supported by the National Natural Science Foundation of China (Nos. 21373208, 91545204, 21688102, and 21621063), and Ministry of Science and Technology of China (Nos. 2016YFA0200200, 2013CB834603, and 2013CB933100), and the Strategic Priority Research Program of the Chinese Academy of Sciences (No. XDB17020200).

Electronic Supplementary Material: Supplementary material (experimental section, additional HS-LEIS, TEM, HRTEM, EDX-mapping, *in-situ* Raman and PROX data) is available in the online version of this article at <http://dx.doi.org/10.1007/s12274-017-1512-8>.

References

- [1] Lim, B.; Jiang, M. J.; Camargo, P. H. C.; Cho, E. C.; Tao, J.; Lu, X. M.; Zhu, Y. M.; Xia, Y. N. Pd-Pt bimetallic nanodendrites with high activity for oxygen reduction. *Science* **2009**, *324*, 1302–1305.
- [2] Yu, W. T.; Porosoff, M. D.; Chen, J. G. Review of Pt-based bimetallic catalysis: From model surfaces to supported catalysts. *Chem. Rev.* **2012**, *112*, 5780–5817.
- [3] Fu, Q.; Li, W. X.; Yao, Y. X.; Liu, H. Y.; Su, H. Y.; Ma, D.; Gu, X. K.; Chen, L. M.; Wang, Z.; Zhang, H. et al. Interface-confined ferrous centers for catalytic oxidation. *Science* **2010**, *328*, 1141–1144.
- [4] Joo, S. H.; Park, J. Y.; Tsung, C. K.; Yamada, Y.; Yang, P. D.; Somorjai, G. A. Thermally stable Pt/mesoporous silica core-shell nanocatalysts for high-temperature reactions. *Nat. Mater.* **2009**, *8*, 126–131.
- [5] Gu, J.; Zhang, Z. Y.; Hu, P.; Ding, L. P.; Xue, N. H.; Peng, L. M.; Guo, X. F.; Lin, M.; Ding, W. P. Platinum nanoparticles encapsulated in MFI zeolite crystals by a two-step dry gel conversion method as a highly selective hydrogenation catalyst. *ACS Catal.* **2015**, *5*, 6893–6901.
- [6] Chen, S. G.; Wei, Z. D.; Qi, X. Q.; Dong, L. C.; Guo, Y. G.; Wan, L. J.; Shao, Z. G.; Li, L. Nanostructured polyaniline-decorated Pt/C@PANI core-shell catalyst with enhanced durability and activity. *J. Am. Chem. Soc.* **2012**, *134*, 13252–13255.
- [7] Cheng, X.; Shi, Z.; Glass, N.; Zhang, L.; Zhang, J. J.; Song, D. T.; Liu, Z.-S.; Wang, H. J.; Shen, J. A review of PEM hydrogen fuel cell contamination: Impacts, mechanisms, and mitigation. *J. Power Sources* **2007**, *165*, 739–756.
- [8] Li, Q. F.; He, R. H.; Gao, J.-A.; Jensen, J. O.; Bjerrum, N. J. The CO poisoning effect in PEMFCs operational at temperatures up to 200 °C. *J. Electrochem. Soc.* **2003**, *150*, A1599–A1605.
- [9] Rodriguez, J. A.; Hrbek, J. Interaction of sulfur with well-defined metal and oxide surfaces: Unraveling the mysteries behind catalyst poisoning and desulfurization. *Acc. Chem. Res.* **1999**, *32*, 719–728.
- [10] Nakamura, H.; Iwama, H.; Yamamoto, Y. Palladium- and platinum-catalyzed addition of aldehydes and imines with allylstannanes. Chemoselective allylation of imines in the presence of aldehydes. *J. Am. Chem. Soc.* **1996**, *118*, 6641–6647.
- [11] Kahlich, M. J.; Gasteiger, H. A.; Behm, R. J. Kinetics of the selective CO oxidation in H_2 -rich gas on Pt/ Al_2O_3 . *J. Catal.* **1997**, *171*, 93–105.
- [12] Lee, I.; Delbecq, F.; Morales, R.; Albitzer, M. A.; Zaera, F. Tuning selectivity in catalysis by controlling particle shape. *Nat. Mater.* **2009**, *8*, 132–138.
- [13] Liu, Z. F.; Hu, J. E.; Wang, Q.; Gaskell, K.; Frenkel, A. I.; Jackson, G. S.; Eichhorn, B. PtMo alloy and MoO_x @Pt core-shell nanoparticles as highly CO-tolerant electrocatalysts. *J. Am. Chem. Soc.* **2009**, *131*, 6924–6925.
- [14] Du, X. X.; He, Y.; Wang, X. X.; Wang, J. N. Fine-grained and fully ordered intermetallic PtFe catalysts with largely enhanced catalytic activity and durability. *Energy Environ. Sci.* **2016**, *9*, 2623–2632.

- [15] Wang, Q. M.; Chen, S. G.; Shi, F.; Chen, K.; Nie, Y.; Wang, Y.; Wu, R.; Li, J.; Zhang, Y.; Ding, W. et al. Structural evolution of solid Pt nanoparticles to a hollow PtFe alloy with a Pt-skin surface via space-confined pyrolysis and the nanoscale kirkendall effect. *Adv. Mater.* **2016**, *28*, 10673–10678.
- [16] Chung, D. Y.; Jun, S. W.; Yoon, G.; Kwon, S. G.; Shin, D. Y.; Seo, P.; Yoo, J. M.; Shin, H.; Chung, Y. H.; Kim, H. et al. Highly durable and active PtFe nanocatalyst for electrochemical oxygen reduction reaction. *J. Am. Chem. Soc.* **2015**, *137*, 15478–15485.
- [17] Kuttiyiel, K. A.; Sasaki, K.; Choi, Y.; Su, D.; Liu, P.; Adzic, R. R. Nitride stabilized PtNi core-shell nanocatalyst for high oxygen reduction activity. *Nano Lett.* **2012**, *12*, 6266–6271.
- [18] Zhai, Q. G.; Xie, S. J.; Fan, W. Q.; Zhang, Q. H.; Wang, Y.; Deng, W. P.; Wang, Y. Photocatalytic conversion of carbon dioxide with water into methane: Platinum and copper(i) oxide co-catalysts with a core-shell structure. *Angew. Chem., Int. Ed.* **2013**, *52*, 5776–5779.
- [19] Hunt, S. T.; Milina, M.; Alba-Rubio, A. C.; Hendon, C. H.; Dumesic, J. A.; Román-Leshkov, Y. Self-assembly of noble metal monolayers on transition metal carbide nanoparticle catalysts. *Science* **2016**, *352*, 974–978.
- [20] Shi, Y.-S.; Yuan, Z.-F.; Wei, Q.; Sun, K.-Q.; Xu, B.-Q. Pt-FeO_x/SiO₂ catalysts prepared by galvanic displacement show high selectivity for cinnamyl alcohol production in the chemoselective hydrogenation of cinnamaldehyde. *Catal. Sci. Technol.* **2016**, *6*, 7033–7037.
- [21] Tang, H. L.; Wei, J. K.; Liu, F.; Qiao, B. T.; Pan, X. L.; Li, L.; Liu, J. Y.; Wang, J. H.; Zhang, T. Strong metal-support interactions between gold nanoparticles and nonoxides. *J. Am. Chem. Soc.* **2016**, *138*, 56–59.
- [22] Fu, Q.; Wagner, T. Interaction of nanostructured metal overlayers with oxide surfaces. *Surf. Sci. Rep.* **2007**, *62*, 431–498.
- [23] Ma, Z.; Dai, S. Design of novel structured gold nanocatalysts. *ACS Catal.* **2011**, *1*, 805–818.
- [24] Wu, Z. X.; Lv, Y. Y.; Xia, Y. Y.; Webley, P. A.; Zhao, D. Y. Ordered mesoporous platinum@graphitic carbon embedded nanophase as a highly active, stable, and methanol-tolerant oxygen reduction electrocatalyst. *J. Am. Chem. Soc.* **2012**, *134*, 2236–2245.
- [25] Lu, J. L.; Fu, B. S.; Kung, M. C.; Xiao, G. M.; Elam, J. W.; Kung, H. H.; Stair, P. C. Coking- and sintering-resistant palladium catalysts achieved through atomic layer deposition. *Science* **2012**, *335*, 1205–1208.
- [26] Guo, L.; Jiang, W.-J.; Zhang, Y.; Hu, J.-S.; Wei, Z.-D.; Wan, L.-J. Embedding Pt nanocrystals in N-doped porous carbon/carbon nanotubes toward highly stable electrocatalysts for the oxygen reduction reaction. *ACS Catal.* **2015**, *5*, 2903–2909.
- [27] Yao, Y. X.; Fu, Q.; Zhang, Y. Y.; Weng, X. F.; Li, H.; Chen, M. S.; Jin, L.; Dong, A. Y.; Mu, R. T.; Jiang, P. et al. Graphene cover-promoted metal-catalyzed reactions. *Proc. Natl. Acad. Sci. USA* **2014**, *111*, 17023–17028.
- [28] Zhang, Y. H.; Weng, X. F.; Li, H.; Li, H. B.; Wei, M. M.; Xiao, J. P.; Liu, Z.; Chen, M. S.; Fu, Q.; Bao, X. H. Hexagonal boron nitride cover on Pt(111): A new route to tune molecule-metal interaction and metal-catalyzed reactions. *Nano Lett.* **2015**, *15*, 3616–3623.
- [29] Zhang, H.; Fu, Q.; Cui, Y.; Tan, D. L.; Bao, X. H. Growth mechanism of graphene on Ru(0001) and O₂ adsorption on the graphene/Ru(0001) surface. *J. Phys. Chem. C* **2009**, *113*, 8296–8301.
- [30] Wei, M. M.; Fu, Q.; Wu, H.; Dong, A. Y.; Bao, X. H. Hydrogen intercalation of graphene and boron nitride monolayers grown on Pt (111). *Top. Catal.* **2016**, *59*, 543–549.
- [31] Gao, L. J.; Fu, Q.; Wei, M. M.; Zhu, Y. F.; Liu, Q.; Crumlin, E.; Liu, Z.; Bao, X. H. Enhanced nickel-catalyzed methanation confined under hexagonal boron nitride shells. *ACS Catal.* **2016**, *6*, 6814–6822.
- [32] Yang, Y.; Fu, Q.; Wei, M. M.; Bluhm, H.; Bao, X. H. Stability of BN/metal interfaces in gaseous atmosphere. *Nano Res.* **2015**, *8*, 227–237.
- [33] Fu, Q.; Bao, X. H. Surface chemistry and catalysis confined under two-dimensional materials. *Chem. Soc. Rev.*, in press, DOI: 10.1039/c6cs00424e.
- [34] Kovtyukhova, N. I.; Wang, Y. X.; Berkdemir, A.; Cruz-Silva, R.; Terrones, M.; Crespi, V. H.; Mallouk, T. E. Non-oxidative intercalation and exfoliation of graphite by Brønsted acids. *Nat. Chem.* **2014**, *6*, 957–963.
- [35] Sutter, P.; Sadowski, J. T.; Sutter, E. A. Chemistry under cover: Tuning metal-graphene interaction by reactive intercalation. *J. Am. Chem. Soc.* **2010**, *132*, 8175–8179.
- [36] Deng, D. H.; Novoselov, K. S.; Fu, Q.; Zheng, N. F.; Tian, Z. Q.; Bao, X. H. Catalysis with two-dimensional materials and their heterostructures. *Nat. Nanotechnol.* **2016**, *11*, 218–230.
- [37] Ferrighi, L.; Datteo, M.; Fazio, G.; Di Valentin, C. Catalysis under cover: Enhanced reactivity at the interface between (doped) graphene and anatase TiO₂. *J. Am. Chem. Soc.* **2016**, *138*, 7365–7376.
- [38] Zhou, Y. N.; Chen, W.; Cui, P.; Zeng, J.; Lin, Z. N.; Kaxiras, E.; Zhang, Z. Y. Enhancing the hydrogen activation reactivity of nonprecious metal substrates via confined catalysis underneath graphene. *Nano Lett.* **2016**, *16*, 6058–6063.
- [39] Emmez, E.; Yang, B.; Shaikhutdinov, S.; Freund, H.-J. Permeation of a single-layer SiO₂ membrane and chemistry in confined space. *J. Phys. Chem. C* **2014**, *118*, 29034–29042.

- [40] Shrestha, R. P.; Diyabalanage, H. V. K.; Semelsberger, T. A.; Ott, K. C.; Burrell, A. K. Catalytic dehydrogenation of ammonia borane in non-aqueous medium. *Int. J. Hydrogen Energy* **2009**, *34*, 2616–2621.
- [41] Smythe, N. C.; Gordon, J. C. Ammonia borane as a hydrogen carrier: Dehydrogenation and regeneration. *Eur. J. Inorg. Chem.* **2010**, *2010*, 509–521.
- [42] Kim, G.; Jang, A. R.; Jeong, H. Y.; Lee, Z.; Kang, D. J.; Shin, H. S. Growth of high-crystalline, single-layer hexagonal boron nitride on recyclable platinum foil. *Nano Lett.* **2013**, *13*, 1834–1839.
- [43] Müller, F.; Grandthyll, S. Monolayer formation of hexagonal boron nitride on Ag(001). *Surf. Sci.* **2013**, *617*, 207–210.
- [44] Xie, Y. P.; Liu, G.; Lu, G. Q.; Cheng, H. M. Boron oxynitride nanoclusters on tungsten trioxide as a metal-free cocatalyst for photocatalytic oxygen evolution from water splitting. *Nanoscale* **2012**, *4*, 1267–1270.
- [45] Wang, Y. J.; Trenary, M. Surface chemistry of boron oxidation. 2. The reactions of boron oxides B₂O₃ and B₂O₅ with boron films grown on tantalum(110). *Chem. Mater.* **1993**, *5*, 199–205.
- [46] Moussa, G.; Moury, R.; Demirci, U. B.; Miele, P. Borates in hydrolysis of ammonia borane. *Int. J. Hydrogen Energy* **2013**, *38*, 7888–7895.
- [47] Yang, F.; Li, Y. Z.; Chu, W.; Li, C.; Tong, D. G. Mesoporous Co–B–N–H nanowires: Superior catalysts for decomposition of hydrous hydrazine to generate hydrogen. *Catal. Sci. Technol.* **2014**, *4*, 3168–3179.
- [48] Sheng, Z. H.; Shao, L.; Chen, J. J.; Bao, W. J.; Wang, F. B.; Xia, X. H. Catalyst-free synthesis of nitrogen-doped graphene via thermal annealing graphite oxide with melamine and its excellent electrocatalysis. *ACS Nano* **2011**, *5*, 4350–4358.
- [49] Brongersma, H. H.; Draxler, M.; De Ridder, M.; Bauer, P. Surface composition analysis by low-energy ion scattering. *Surf. Sci. Rep.* **2007**, *62*, 63–109.
- [50] Yu, X. W.; Ye, S. Y. Recent advances in activity and durability enhancement of Pt/C catalytic cathode in PEMFC: Part II: Degradation mechanism and durability enhancement of carbon supported platinum catalyst. *J. Power Sources* **2007**, *172*, 145–154.
- [51] Antolini, E. Carbon supports for low-temperature fuel cell catalysts. *Appl. Catal. B: Environ.* **2009**, *88*, 1–24.
- [52] Deng, D. H.; Pan, X. L.; Zhang, H.; Fu, Q.; Tan, D. L.; Bao, X. H. Freestanding graphene by thermal splitting of silicon carbide granules. *Adv. Mater.* **2010**, *22*, 2168–2171.
- [53] Albitzer, M. A.; Crooks, R. M.; Zaera, F. Adsorption of carbon monoxide on dendrimer-encapsulated platinum nanoparticles: Liquid versus gas phase. *J. Phys. Chem. Lett.* **2010**, *1*, 38–40.
- [54] Mu, R. T.; Fu, Q.; Jin, L.; Yu, L.; Fang, G. Z.; Tan, D. L.; Bao, X. H. Visualizing chemical reactions confined under graphene. *Angew. Chem., Int. Ed.* **2012**, *51*, 4856–4859.
- [55] Grånäs, E.; Andersen, M.; Arman, M. A.; Gerber, T.; Hammer, B.; Schnadt, J.; Andersen, J. N.; Michely, T.; Knudsen, J. Co intercalation of graphene on Ir(111) in the millibar regime. *J. Phys. Chem. C* **2013**, *117*, 16438–16447.
- [56] Ma, D. L.; Zhang, Y. F.; Liu, M. X.; Ji, Q. Q.; Gao, T.; Zhang, Y.; Liu, Z. F. Clean transfer of graphene on Pt foils mediated by a carbon monoxide intercalation process. *Nano Res.* **2013**, *6*, 671–678.
- [57] Jin, L.; Fu, Q.; Dong, A. Y.; Ning, Y. X.; Wang, Z. J.; Bluhm, H.; Bao, X. H. Surface chemistry of CO on Ru(0001) under the confinement of graphene cover. *J. Phys. Chem. C* **2014**, *118*, 12391–12398.
- [58] Wei, M. M.; Fu, Q.; Yang, Y.; Wei, W.; Crumlin, E.; Bluhm, H.; Bao, X. H. Modulation of surface chemistry of CO on Ni(111) by surface graphene and carbide carbon. *J. Phys. Chem. C* **2015**, *119*, 13590–13597.
- [59] Kim, H.; Robertson, A. W.; Kim, S. O.; Kim, J. M.; Warner, J. H. Resilient high catalytic performance of platinum nanocatalysts with porous graphene envelope. *ACS Nano* **2015**, *9*, 5947–5957.
- [60] Dong, A. Y.; Fu, Q.; Wu, H.; Wei, M. M.; Bao, X. H. Factors controlling the CO intercalation of h-BN overlayers on Ru(0001). *Phys. Chem. Chem. Phys.* **2016**, *18*, 24278–24284.
- [61] Wen, Z. H.; Liu, J.; Li, J. H. Core/shell Pt/C nanoparticles embedded in mesoporous carbon as a methanol-tolerant cathode catalyst in direct methanol fuel cells. *Adv. Mater.* **2008**, *20*, 743–747.
- [62] Gao, L. J.; Fu, Q.; Li, J. M.; Qu, Z. P.; Bao, X. H. Enhanced CO oxidation reaction over Pt nanoparticles covered with ultrathin graphitic layers. *Carbon* **2016**, *101*, 324–330.
- [63] Mievile, R. L.; Reichmann, M. G. Temperature-programmed desorption study of CO on Pt-reforming catalysts. In *Characterization and Catalyst Development, ACS Symposium Series*; American Chemical Society: Washington, DC, 1989; Vol. 411, pp 243–250.
- [64] Patience, G. S.; Benamer, A.; Chiron, F. X.; Shekari, A.; Dubois, J. L. Selectively combusting CO in the presence of propylene. *Chem. Eng. Process.: Process Intensification* **2013**, *70*, 162–168.
- [65] Binder, A. J.; Toops, T. J.; Unocic, R. R.; Parks, J. E., II; Dai, S. Low-temperature CO oxidation over a ternary oxide catalyst with high resistance to hydrocarbon inhibition. *Angew. Chem., Int. Ed.* **2015**, *54*, 13263–13267.